Featured in Physics

Towards a Pseudocapacitive Battery: Benchmarking the Capabilities of Quantized Capacitance for Energy Storage

Yee Wei Foong,[1,*] Javad Shirani,[1] Shuaishuai Yuan,[1] Christopher A. Howard,[2] and Kirk H. Bevan[1,3,†]

[1] *Division of Materials Engineering, Faculty of Engineering, McGill University, Montréal, Québec H3A 0C5, Canada*

[2] *Department of Physics and Astronomy, University College London, London, United Kingdom*

[3] *Centre for the Physics of Materials, Department of Physics, McGill University, Montréal, Québec H3A 2T8, Canada*

(Received 14 January 2022; revised 22 April 2022; accepted 11 May 2022; published 23 June 2022)

Despite being capable of very fast charging, the pseudocapacitive properties of electrochemical capacitors still require significant research to attain energy densities comparable to that of batteries. Herein we discuss and theoretically benchmark the physics of quantized capacitance as a Faradaic charge storage mechanism, providing near "ideal" pseudocapacitive properties in the context of batterylike energy storage. Through careful electrolyte and reactant engineering, our physical analysis suggests that this less explored "pseudocapacitive battery" mechanism could provide power densities of approximately 10^4 W/L combined with volumetric energy densities in the range of 100 Wh/L (or potentially greater). These benchmarks are arrived at though a comprehensive analysis of two-dimensional (2D) graphitic nanoparticles considering the impact of solvation, electron-electron interactions, and electron transfer processes. In general, our findings indicate that 2D nanomaterials exhibiting quantized capacitance provide a promising and underexplored physical axis within electrochemical capacitors towards realizing very fast charging at energy densities comparable to that of batteries.

DOI: 10.1103/PRXEnergy.1.013007

I. INTRODUCTION

Electrochemical capacitors combine both electric double layer (EDL) and Faradaic mechanisms to maintain high power densities, but at energy densities that exceed the performance of purely EDL-based capacitors. This improvement is often accomplished by utilizing redox-active nanoparticles at the electrode surface, which store additional electrons in a Faradaic manner that mimics EDL charge storage "pseudocapacitively." It is the ultimate goal of this effort to maintain the high power performance of electrochemical capacitors while pushing towards the energy density regime typically occupied by batteries [1, 2]. A great deal of research is currently focused on realizing a high performance pseudocapacitance energy storage enabled by nanomaterials [3–6]. However, despite extensive experimental activity, the physics which underlie a pseudocapacitive response in a given nanomaterial system are not well understood [7–9]. Recently, it was proposed that suitably engineered conducting nanoparticles might be tailored to exhibit a near ideal pseudocapacitive response through the use of "quantized capacitance"—an observable Faradaic mechanism in nanoparticles arising from electron-electron interactions related to Coulomb blockade [10–17]. However, the energy and power density capabilities of "quantized capacitance" have yet to be fully explored. Herein, we seek to theoretically benchmark the maximum energy and power density storage capabilities for an electrochemical system making use of quantized capacitance and its promising pseudocapacitive features. Through our analysis we are able to show that quantized capacitance can, theoretically, provide the combination of high power density and energy density long sought by the field [1].

In Fig. 1 the approximate power and energy density performance of various energy storage technologies are provided in the form of a Ragone plot. The highest power density is provided by conventional capacitors (red, Fig. 1), though they suffer from very low-energy storage

*yeewei.foong@mail.mcgill.ca
†kirk.bevan@mcgill.ca

Published by the American Physical Society under the terms of the Creative Commons Attribution 4.0 International license. Further distribution of this work must maintain attribution to the author(s) and the published article's title, journal citation, and DOI.

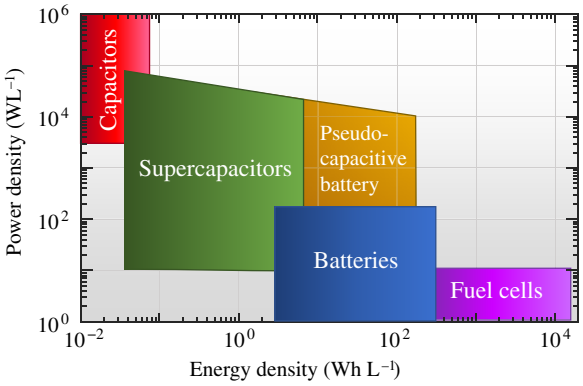

FIG. 1. (Adapted from Ref. [1].) A Ragone plot depicting the volumetric power and energy densities of various energy storage devices. Theoretical energy storage benchmarks for a "pseudocapacitive battery" operating via quantized capacitance (gold region) are discussed and presented in this manuscript.

density. In supercapacitors, the EDL mechanism is tailored through multiscale nanostructuring to maintain a comparatively high power density while extending towards volumetric energy densities of the order of 10 Wh/L (green, Fig. 1) [18,19]. On the other hand, conventional batteries provide much better energy storage than supercapacitors but typically at a much lower power density [20–22]. The driving impetus, behind engineering a pseudocapacitive component within an electrochemical capacitor, is to maintain the fast charging properties of supercapacitors while extending performance towards the energy densities currently occupied by batteries [3–6,18,19]. This long standing nexus is shown in gold in Fig. 1, our specific aim is to assess the degree to which "quantized capacitance" might be engineered to yield both high power and energy densities within this region resulting in a "pseudocapacitive battery."

Our investigation is motivated by recent promising developments in the usage of graphitic nanoparticles, where they have been utilized electrochemically to great effect by tuning both their dimensionality and laminate packing [23,24]. It has also been shown that carbon nanostructures can store high densities of electrons [23–28]. Additionally, from a pseudocapacitive perspective graphite or graphene is intriguing, since it is a bulk conductor, which through sufficient nanostructuring can provide "quantized capacitance" charging states that are accessible electrochemically [12,29–31]. Moreover, graphitic nanoparticles can be resolved down to one atomic layer and such that all atoms equally participate in charge storage. That is, there is no internal region in such a two-dimensional (2D) material and therefore the charge storage as a function solely of the nanoparticle volume is maximized—compared to say a conducting sphere, where net charge aggregates towards the surface. Driven by these developments we utilize the proposed "quantized capacitance" energy storage scheme in Fig. 2(a) to benchmark its performance within the gold region highlighted in Fig. 1. Though quantized capacitance has been investigated experimentally at dilute concentrations, exhibiting intriguing multiple redox and amphoteric properties [12,29,31,32], its ultimate theoretical potential as an energy storage mechanism at high packing densities has not been explored.

The fully charged configuration within this storage scheme is provided in Fig. 2(a), where the negative electrode holds electrons (e^-) taken from the positive electrode to leave behind holes (h^+, the absence of an electron). Screening counterions must be present within both electrodes in equal concentration to their stored charges, as shown in blue and red in Fig. 2(a), to prevent the onset of Coulomb explosion [33,34]. Likewise, the discharging state is illustrated in Fig. 2(a), where electrons placed on the negative terminal move back over to the positive terminal and counterions diffuse accordingly in the opposite direction. Apart from the use of quantized graphitic nanoparticles, the scheme in Fig. 2(a) is operationally quite similar to that of a redox-polymer battery as juxtaposed in Fig. 2(b) [22,35–37]. The two schemes are analogous in several respects: (1) redox processes occur throughout both the positive and negative terminal charging media; (2) electrons are stored on the negative terminal and holes on the positive terminal; (3) the diffusion of electron and holes is facilitated by intersite electron transfer; and (4) counterions are allowed to freely diffuse to prevent the onset of Coulomb explosion [22,33,35–37]. However, the use of quantized nanoparticles enables two key additional features: (1) the charge stored at a given voltage can be tuned through dimensionality engineering; and (2) multiple redox events occur at each site through the use of quantized capacitance [10,29,31]. This latter difference is key as it enables a near "ideal" pseudocapacitive behavior in such nanoparticles, in direct contrast to the peaked voltammetric behavior found in a redox-polymer battery—contrast the lower green voltammogram in Fig. 2(a) with the lower orange voltammogram in Fig. 2(b). Indeed, one might consider the proposed mechanism in Fig. 2(a) to be that of a "pseudocapacitive battery."

To explore the physical feasibility of such a "quantized capacitance" storage mechanism, of the form presented in Fig. 2(a), our analysis is divided into several parts. First, we explore the volumetric energy density limits that would be provided by this scheme in Sec. II. This encompasses a discussion on the general electron storage capabilities in Sec. II A, followed by an overview on the quantized capacitance redox mechanism in Sec. II B and its operational voltage tuning capabilities in Sec. II C. Our volumetric energy density assessment concludes with a consideration of how electrolyte stability impacts upon energy storage via this mechanism in Sec. II D. Then in Sec. III we address how the power performance targeted in

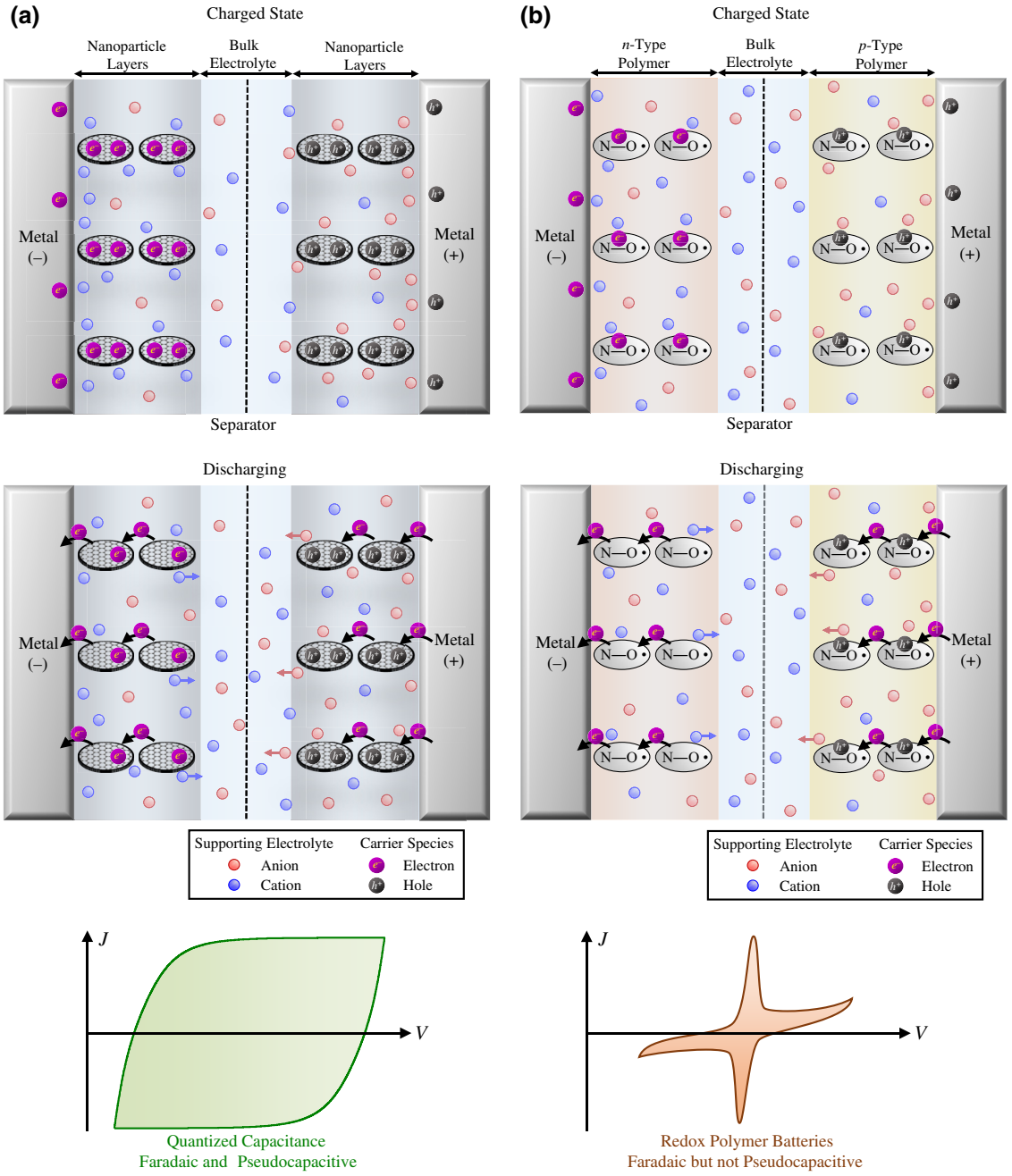

FIG. 2. (a) Operational schematic for a quantized capacitance device similar to (b) (adapted from Ref. [22]) a redox-polymer battery. Both schemes are depicted in the fully charged state and during discharging. Their corresponding cyclic voltammograms are illustrated in the bottom panel of each subfigure. In a quantized capacitance device, graphitic nanoparticles with negative charge states are utilized to store electrons during charging, while graphitic nanoparticles with positive charge states are utilized for electron (e^-) stripping for charge counter balancing. Here, the stripping or removal of electrons (to realize positively charged states) is denoted by "holes" (h^+)—just as it is in a redox-polymer battery. This design is provided to explore the possible capabilities of the mechanism; more advanced multiscale designs to aid charge carrier diffusion and transport will likely be important in any practical implementation [38–40]. Redox-based flow battery analogues may also be similarly applied [41–43].

Fig. 1 might be achieved. Lastly, in Sec. IV we discuss the relevance of "quantized capacitance" to similar technologies (such as redox-polymer batteries) and summarize our findings. It is important to emphasize that our goal throughout is to assess the general physical possibility of such a storage mechanism; not to delve into highly system-specific electrolyte, packing, or other engineering parameters.

II. VOLUMETRIC ENERGY DENSITY

A. General energy storage design concepts

Fundamentally, the volumetric energy storage density of a system is a product of the density at which electrons are stored and the voltage V at which they are placed. In a capacitive system this is summarized by $E = \frac{1}{2}CV^2 = \frac{1}{2}QV$, where C is the capacitance and Q is the charge stored ($Q = CV$) [44,45]. Since we are considering nanoscale graphene disks in our model system [see Fig. 2(a)], this energy storage density is then proportional to the number of electrons stored in such nanodisks. Although our manuscript discusses energy storage design within the context of a graphitic nanodisk-based system, the approach discussed below can also be applied to a range of similar nanomaterials [46–49]. However, nanodisks are likely advantageous as they utilize a minimal amount of pseudocapacitive volume to store charge (having no "interior region," for example compared to spherical nanoparticles).

Recent measurements have shown that nanoscale graphitic systems can store one electron for approximately every ten carbon atoms [23,24]. This achievable ratio, when applied to graphene or nanodisks thereof, results in a surface electron storage density of $\sigma_e \approx 4$ q/nm^2—where $q = 1.6 \times 10^{-19}$ C is the elementary charge. Although this electron density is less than the theoretical maximum of fully intercalated graphite in batteries [50–52], it is still a significant storage density for supercapacitor systems. To induce quantized capacitance, a nanoparticle must be separated from other similar particles by a supporting medium [10,11,17,23,53], since this promotes electron-electron interactions and enables one to tune the storage voltage, as will be discussed in Sec. II B. The dielectric properties of this insulating medium, which is quite often an electrolyte, also impact upon the voltage storage properties associated with quantized capacitance [10,17,54]—a topic to be discussed in depth shortly as well. Thus, when combining our model graphene nanodisks with a supporting medium separating them, which can be as thin as 1 nm [10,17,55], one obtains the electron density trend presented in Fig. 3(a). It is critical that one assess the electrolyte fraction present in the porous electrode because, to arrive at a plausible energy storage technology, the packing density of nanoparticles must be increased compared to existing scientific studies of quantized capacitance [11,29]. This is needed to achieve high volumetric energy densities via this mechanism, similar to how the molar concentration of redox species should be increased to achieve higher volumetric energy density in a flow battery. Here we have assumed an effective thickness for a graphene nanodisk corresponding to $d \approx 0.4$ nm, roughly equal to the spacing between graphite sheets [23,24], and have varied the total volume from 2 times to 20 times the reactant (nanodisks) volume. Accordingly, at a storage voltage of $V_d = 5$ V, one then obtains the volumetric energy density trends presented in Fig. 3(a) that can be described by

$$E_d = \frac{1}{4}\left(\frac{qV_d\sigma_e}{d+L}\right). \tag{1}$$

Here L is the thickness of the supporting medium region relative to the disk region—a parameter obtainable by summing all the nanodisks as a "single surface" and placing it atop the volume of the entire supporting medium normalized to the same surface area [see Fig. 3(b)]. Note that a factor of $\frac{1}{4}$ is appended to the energy density expression in Eq. (1). The first $\frac{1}{2}$ multiplier in this contribution arises from the equal volume of opposite charge that must be stored at the cathode [see Fig. 2(a)]. The second $\frac{1}{2}$ multiplier arises from the manner in which charge is stored via quantized capacitance, being added in equal degrees at higher and lower voltages for a given terminal just like a regular capacitor [10,17,54]—further discussion can be found in the Supplemental Material [56]. From Fig. 3(a), it can be seen that when half of the volume is electroactive, we obtain the upper Ragone energy density limit of about 250 Wh/L for quantized capacitance, as shown in Fig. 1. On the other hand, the energy density is significantly degraded when the overall volume is 20 times greater than the electroactive contribution—leading to the lower limit provided in Fig. 1. The higher extreme of about 250 Wh/L is likely unrealistic and the lower limit is likely impractical, but arguably intermediate densities around 100 Wh/L are theoretically achievable, as we will explore further below.

B. Mechanisms giving rise to quantized capacitance

Our primary energy density assumption in Figs. 1 through 3 is that the redox potentials of nanoparticles exhibiting quantized capacitance can be pushed towards encompassing a bias window of near 5 V. This is arguably the maximum achievable bias window for most state-of-the-art electrolyte systems [57–60]. Here we detail how energy storage at this voltage "limit" might be accomplished via quantized capacitance. A detailed description of quantized capacitance as a pseudocapacitive mechanism has previously been published in Ref. [10]. Readers who are familiar with this topic can proceed to Sec. II C and thereafter, where the main contributions of this manuscript are discussed. Nevertheless, we briefly describe the quantized capacitance mechanism in this section for the benefit of a broad readership.

When an electrode is biased towards electron storage in the manner shown on the left-hand side of Fig. 2(a), the potential difference will raise the Fermi energy level in the electrode relative to nanoparticles in the electrolyte,

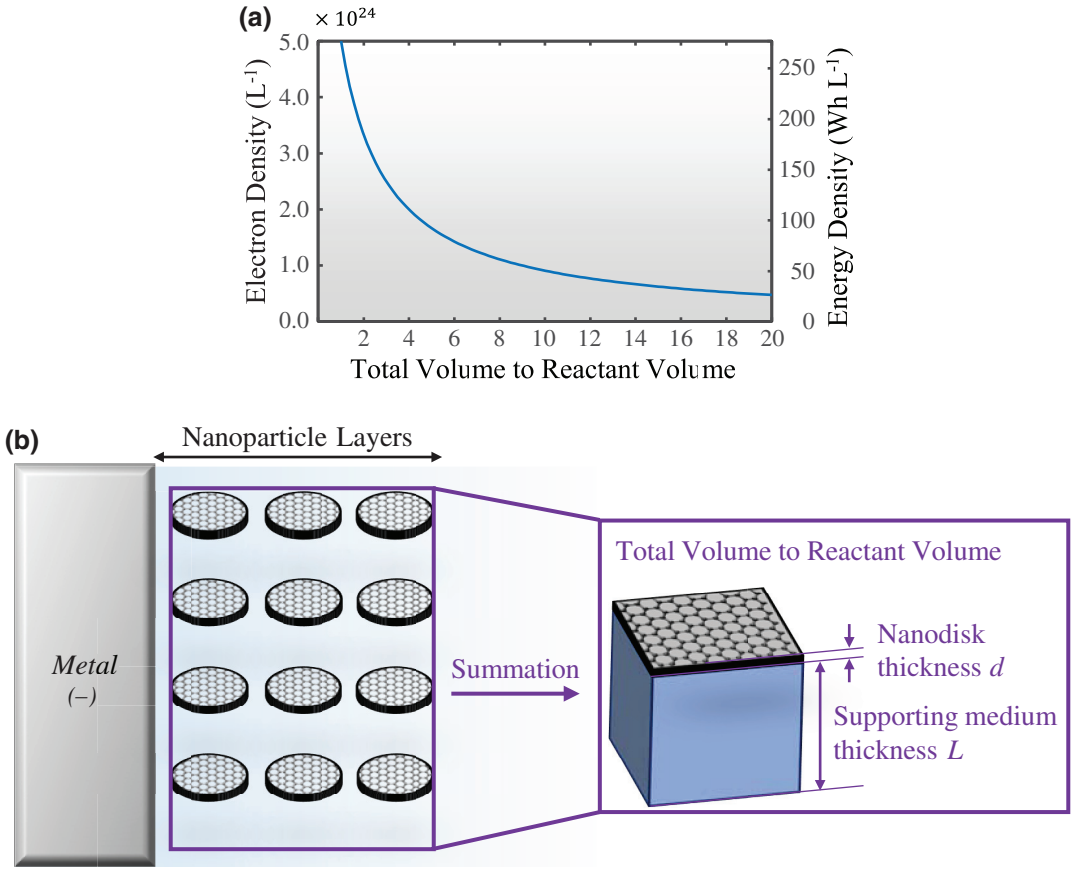

FIG. 3. (a) Electron density as a function of the ratio of total volume to reactant (nanodisks) volume, assuming a surface electron storage density of 4 q/nm^2 and the corresponding volumetric energy density at 5 V storage voltage. (b) A schematic that shows the total volume to reactant (nanodisks) volume can be calculated by taking the ratio of the nanodisk thickness d and the supporting medium thickness L.

as shown in Fig. 4. This bias will then initiate electron transfer into the unoccupied electronic states present in the nanoparticles [see Fig. 4(b)]. Because of the limited size of the nanoparticles, each electron being added will experience measurable electron-electron repulsion, leading to the initial charging energy cost U_o that constitutes quantized capacitive behavior [10–17]. For a nanodisk, this charging energy cost U_o can be approximately expressed as [10,61]

$$U_o = \frac{q^2}{2\pi\epsilon_{\mathrm{op}}\epsilon_o r}F(r). \tag{2}$$

Here, ϵ_o is the permittivity of vacuum, ϵ_{op} is the optical dielectric constant, and r is the nanoparticle radius. The function $F(r)$ accounts for the average electrostatic potential across a uniformly charged disk—a detailed explanation of this expression can be found in the Supplemental Material [56]; see also Ref [61]. After solvent reorganization the placement of the electron reduces to U, which includes orientational dielectric contributions present in liquid electrolyte:

$$U = \frac{q^2}{2\pi\epsilon_r\epsilon_o r}F(r) \tag{3}$$

$$= U_o - 2\lambda. \tag{4}$$

Here ϵ_r is the relative permittivity of the electrolyte and λ is the heterogeneous reorganization energy [17,62,63]. As a result of these interactions, a voltammetric scan will exhibit multiple overlapping electron transfer current peaks separated by U—shown as dashed lines in Fig. 4(a) [10,16,17,64]. By carefully engineering U one can physically tailor the individual redox peaks to sufficient overlap with each other such that a near-rectangular voltammetry profile for pseudocapacitive energy storage behavior is enabled [solid line in Fig. 4(a)] [10].

Importantly, we are considering a tunneling electron transfer process between the electrode and nanoparticle dispersion, as shown in Fig. 2(a) [17,22]. Hence, the multiple redox peaks presented in Fig. 4(b) can

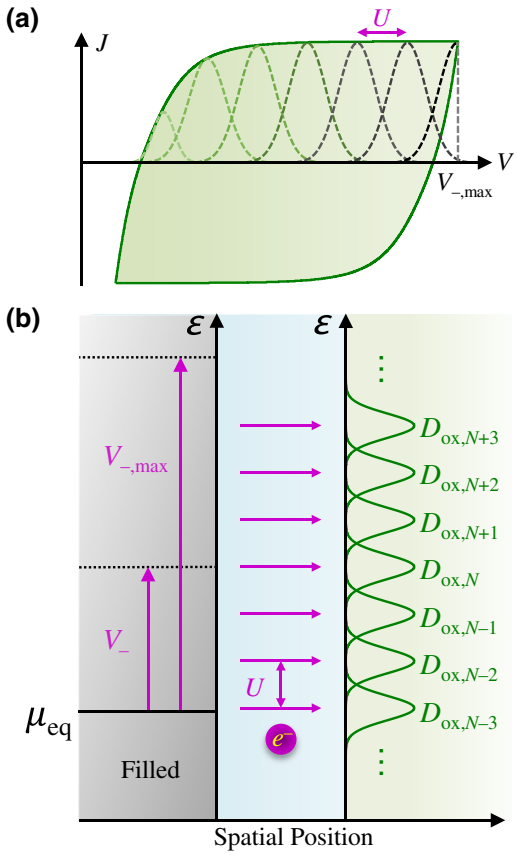

FIG. 4. (Adapted from Ref. [10].) (a) Cyclic voltammetry of quantized capacitance up to a maximum applied potential $V_{-,\max}$ on a single electrode that resembles an ideal pseudocapacitive behavior due to the overlapping electron transfer peaks. (b) A schematic of a single negative (−) electrode depicting the operation of quantized capacitance Faradaic storage via electron tunneling to each reactant state. Here, the schematic describes the electron storage at a cathode during the charging process (as the electrode electrochemical potential $\mu_{\rm eq}$ is raised). At $V_{-,\max}$ the desired electron density is stored. A similar schematic can be used to understand electron removal at the positive (+) terminal during the charging process.

each be described within Gerischer-Hopfield theory [10,63,65–67]. Each electron transfer event into a nanoparticle with N electrons is described by the oxidation distribution

$$D_{{\rm ox},N}(\varepsilon) = \frac{1}{\sqrt{4\pi\lambda k_B T}} \exp\left(\frac{-(\varepsilon - \varepsilon_{{\rm ox},N})^2}{4\lambda k_B T}\right), \quad (5)$$

where ε is the single-particle energy found in the Gerischer-Hopfield framework [10,63,65–67]. Likewise, an electron removal event from a nanoparticle with N electrons occurs via

$$D_{{\rm red},N}(\varepsilon) = \frac{1}{\sqrt{4\pi\lambda k_B T}} \exp\left(\frac{-(\varepsilon - \varepsilon_{{\rm red},N})^2}{4\lambda k_B T}\right), \quad (6)$$

where k_B is the Boltzmann constant and T is the temperature. Moreover, $\varepsilon_{{\rm ox},N}$ is the single-particle energy level of the Nth oxidized state; similarly, $\varepsilon_{{\rm red},N}$ is the single-particle energy level of the Nth reduced state. These single-particle redox levels are then related by [10,53,62]

$$\begin{aligned} \varepsilon_{{\rm red},N+1} - \varepsilon_{{\rm red},N} &= U, \\ \varepsilon_{{\rm ox},N} - \varepsilon_{{\rm red},N+1} &= 2\lambda. \end{aligned} \quad (7)$$

Here it is assumed that wavefunction quantization contributions to the total energy arising from an electron addition or removal event are negligible [10,17]. Crucially, we can engineer λ and U to tune the redox peak placement in a quantized capacitance system to encompass a target $V_{-,\max}$ placement voltage for a given number of electrons [see Fig. 4(b)]. However, overall storage voltage V_d of the system envisioned in Fig. 2(a) is determined by the sum of the maximum potential drop across two such terminals: one biased, as depicted in Fig. 4(b) [forming the negative terminal in Fig. 2(a)], and the other oppositely biased for electron removal [forming the positive terminal in Fig. 2(a)]. The nature of this biasing is a subtle point for consideration that will be discussed in Sec. II D.

C. Tuning the energy storage voltage

From Secs. II A and II B we arrive at two key metrics. First, we would like to arrive at a nanodisk electron storage density of around 4 q/nm^2 for the proposed mechanism in Figs. 1 and 2(a) [23,24]. Second, we need to tune the charging energy parameter U such that this density of electrons is stored and removed at a bias of about 2.5 V on a given terminal relative to the fully discharged state (for a total of about 5 V across both terminals). From Eqs. (2) and (3) we can see that the solvent dielectric constant (ϵ_r) and nanodisk radius (r) are two key physical means for accomplishing this. In Fig. 5(a) we plot the operating voltage at a given terminal as a function of the solvent dielectric constant for several nanodisk radii, all storing electrons at a density of $\sigma_e = 4$ q/nm^2. The total number of electrons stored in a given disk is $\pi r^2 \sigma_e$; this can be coupled with Eqs. (2) and (3) to provide the trends in Fig. 5(a). Because of the reciprocal relation between ϵ_r and U in Eq. (3), an increase in ϵ_r reduces U [see Fig. 5(b)]. This enables a smaller U spacing between consecutive electron transfer peaks, leading to a lower required single electrode voltage $V_{-,\max}$ for a targeted density of charge storage [see Fig. 5(a)]. The maximum density of charge that can be stored is determined by the number of counterions that can packed in to maintain charge neutrality [see Fig. 2(a)] [34]. Ideally, U should also be higher than the thermal energy of about $k_B T$—though this is not a strict necessity. Hence, when tuning the maximum voltage ($V_{-,\max}$), a U value within the range of 0.025 to 0.1 eV is preferable when working to maximize the voltage at

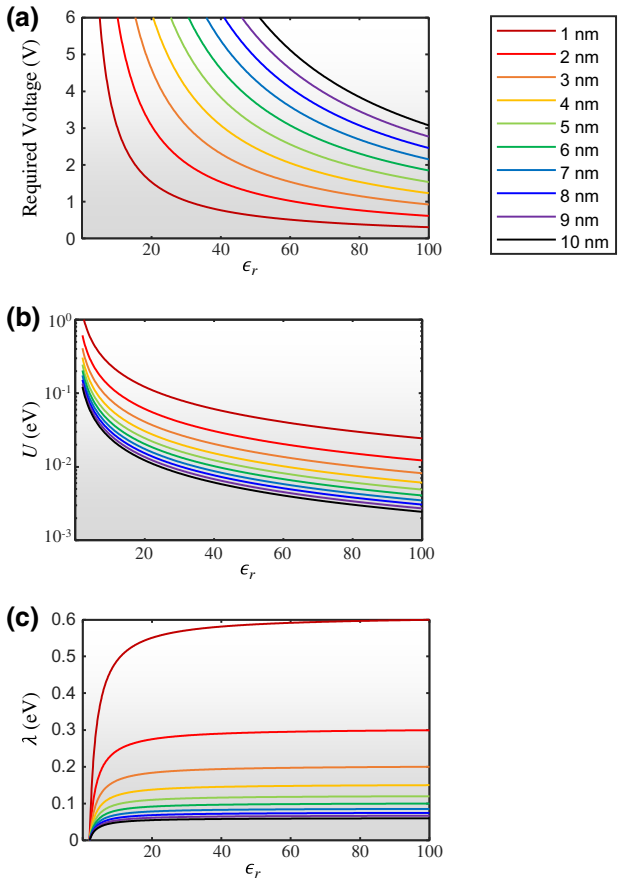

FIG. 5. (a) Achieving a target single electrode voltage for adding a target density of electrons via quantized capacitance by tuning the dielectric response and nanoparticle radius. (b) The change in parameter U in response to tuning the dielectric response and nanoparticle radius as described by Eq. (3). (c) The change in reorganization energy λ with various dielectric responses and nanoparticle radii. Note that (a) is computed with a target density of electrons of 4 q/nm^2.

a high density of electrons storage [10]. Comparing Figs. 5(a) and 5(b) we see that disks with a radii in the range of 3–4 nm within a dielectric medium characterized by ϵ_r between 40–60 would serve well. This would then provide an operating voltage contribution of about 2.5 V per terminal (at $\sigma_e = 4$ q/nm^2) for a total of about 5 V. However, these estimates are derived classically and a more refined search should consider atomic scale interactions, as will be discussed shortly.

The reorganization energy λ of a given particle is also dependent on the radius and dielectric medium of such a nanodisk. Its outer-sphere contribution can be directly computed from Eq. (4) and is plotted as a function of ϵ_r for various nanodisk radii in Fig. 5(c). Here we are assuming that $\epsilon_{op} = 2$. The reorganization energy is important in that it enables a smooth pseudocapacitive current by providing sufficient overlap between many overlapping redox peaks, as governed by Eqs. (3) through (7). If λ is too small relative to U, the ability of this mechanism to provide a smooth capacitive voltammetric profile, such as that in Fig. 4(a), can become hampered, as discussed in Ref. [10]. Hence, ideally, one would like to maintain $\lambda \geq U$. From the results in Fig. 5(c), this should also be satisfied by nanodisks with radii of 3–4 nm within a dielectric medium characterized by ϵ_r between 40–60. The reorganization energy is also an important contributing factor in the power density performance of the energy storage mechanism envisioned in Fig. 2(a), which we will discuss in Sec. III.

Lastly, it is important to recognize that the classical estimates in Fig. 5 exclude: (1) the screening response [68–72] and space charge polarization [73,74] of counterions; and (2) the inner-sphere reorganization response of the solvent electrolyte molecules. Hence, the results in Fig. 5 serve only as an approximate physical estimate. Detailed atomistic calculations are needed to more accurately compute the combined counterion and molecular-scale contributions to the charging and reorganization energies in a given supporting medium [75–77]. However, it has been experimentally demonstrated that a charging energy response should be present at the nanoscale in such a system, as demonstrated in Ref. [78] as well as other works [17,29,31,79]. Hence, the general physical arguments presented should hold—above and beyond system specific details. Overall, the results in this subsection are intended to convey the importance of tailoring both the dielectric medium and nanodisk dimensionality. Both should be tuned to attain a target electron storage density (per disk) at a given storage voltage via the quantized capacitance mechanism.

D. Electrolyte considerations in quantized capacitance

As mentioned briefly in Sec. II B, charge storage via quantized capacitance occurs over two electrodes [see Fig. 2(a)]. One electrode serves as the negative (−) terminal by gaining electrons during charging, while the other serves as the positive (+) terminal by giving up electrons during charging. Since opposite charges are stored on both electrodes, the terminals will be biased in opposite directions with respect to their fully discharged configuration. Hence, the overall cell potential in Eq. (1) is the addition of the biases on both electrodes as described by

$$V_d = |V_{+,\max}| + |V_{-,\max}|. \tag{8}$$

Here, $|V_{+,\max}|$ is the maximum applied bias dropping at the positive terminal and $|V_{-,\max}|$ is that of the negative terminal (see Fig. 4). In the simple case of symmetric electrodes, the biases on both electrodes will be approximately equal such that $|V_{+,\max}| \approx |V_{-,\max}| \approx V_d/2$, as shown in Fig. 6(a). However, it is also possible that the total voltage (V_d) in Eq. (8) may be split asymmetrically across two terminals ($|V_{+,\max}| \neq |V_{-,\max}|$) with each storing an equal amount of charge. Following from the results of Fig. 5, this

asymmetric splitting may occur when the nanodisk radius and/or the supporting medium dielectric response is not the same at both electrodes. For example, suppose that the positive (+) terminal has particles twice (2 times) the radius than those on the negative (−) terminal. Then, keeping all other system parameters fixed, the positive terminal (+) will only require $|V_{+,\max}| = |V_{-,\max}|/2$ to store the same density of electrons (see Fig. 5). Under this scenario, $2V_d/3$ would drop across the negative (−) terminal and $V_d/3$ would drop across the positive (+) terminal. More generally, the manner of voltage splitting matters because it can be utilized to maximize energy storage within electrolyte stability constraints, as we now explore.

This voltage splitting arrangement relates directly to how positive and negative charges can be stored in the manner proposed in Fig. 2(a). It is well known that carbon nanostructures excel at storing electrons [23–25]. Indeed, as mentioned in Sec. II, an electron storage density of about 4 q/nm^2 can be routinely achieved. However, the propensity for electron removal from carbon nanostructures is much more challenging [80,81]. For example, while one can place up to about seven electrons on a C_{60} molecule, only up to three electrons can typically be removed [25,78,80,81]. Whether one is considering fullerenes or another carbon nanostructure, this difficultly arises when the removal of electrons from the electrolyte (breakdown) occurs at an earlier potential than the removal of further electrons from the intended (carbon) nanostructure. On the other hand, it is possible to attain stability upon removal of high densities of electrons in bulk graphitic systems. For example, in BrC_8 graphite sheets give up to about 4.8 q/nm^2 [82]. More recently, similar success has been found in $FeCl_3$-doped graphene [83]. Comparatively, in C_{60} the ratio of electrons that can be removed (even in the presence of counterions) is around one for every 20 atoms, versus one for every eight atoms in BrC_8. The challenge, of course, is how to achieve the excellent electron-electron removal capabilities of graphite or graphene in a smaller nanostructure where the $V_{+,\max}$ storage voltage can be tuned following Sec. II C—prior to reaching electrolyte breakdown.

The contrasting ability of graphite to give up more electrons than C_{60} is due to the energies at which electron removal can be accessed. Since electrons are well delocalized in graphene or graphite, the quantization and electron-electron interaction energetic costs associated with electron removal (or addition) are much less than in C_{60} [10,53,54,69,84]. Consider the comparative electronic structure plots for graphene and C_{60} in Fig. 6(a). Here we can see that the HOMO level of C_{60} lies about 6 eV below vacuum, while the charge neutrality point (Dirac cone) of graphite or graphene lies at about 5 eV below vacuum as calculated from first principles—see the Supplemental Material [56] and also Refs. [85–89]. Now, in Fig. 6(a) we have superimposed in green the stability window of a hypothetical electrolyte ranging from −2 to −7 eV below vacuum. This range is chosen for its potential to be realized through electrolyte engineering methods [58,90–92]; it has also been placed above band structure plots for graphene and BrC_8 decorated graphene [93–95]. Clearly, the removal of all such electrons from single-layer BrC_8 lies within the stability window of this electrolyte [96]. However, assuming a charging energy of $U = 0.3$ eV after the removal of about three electrons from C_{60} we find that the stability limit of the electrolyte is reached [17]. Note that the HOMO level of C_{60} is sixfold degenerate. Hence, beyond the HOMO-LUMO gap only the charging energy contributes to the cost of electron removal of the first six electrons in C_{60} [17,78]. The point here is that it is the dimensionality of graphite (graphene), being a bulk 2D (3D) material, that allows a very high density of electrons to be removed with minimal energetic cost (U). This can be seen in the far right single-layer BrC_8 band structure in Fig. 6(a), where the Fermi (E_f) level lies well above any electrolyte stability considerations. However, in C_{60} the energetic cost of electron removal (U) is much higher and so much less can be removed at the same potential (or any potential prior to electrolyte breakdown). Thus, the dimensionality of a nanostructure directly impacts on the density of charge it can store prior to reaching the voltage limit at which electrolyte breakdown occurs. Conversely, one can maximize the voltage (prior to electrolyte breakdown) at which a target electron density is removed from graphitic nanostructures (e.g., disks) by tuning their dimensionality (see Fig. 4). Intriguingly, the ability to store more electrons within a fixed bias range with increasing radius (and to do so with high amphoteric propensity) has been experimentally demonstrated in graphene nanoparticles via quantized capacitance [29].

To overcome these electrolyte stability issues, which compete with the electron storage and removal, we briefly explore two possible engineering avenues for the system proposed in Fig. 2(a). First, one can attempt to engineer an electrolyte that has a large stability window that is directly symmetric about the Dirac cone of graphene or graphite (at about 5 eV), as shown in Fig. 6(a). In this manner, the charging levels of smaller graphitic nanodisks will also align about the Dirac cone, allowing for the use of symmetrically designed positive and negative terminals with the same disk size, which in turn maximize the storage voltage for the target electron density, as shown in Fig. 6(a). The framework for relating the single-particle ionization and affinity energies (such as the "Dirac cone") in Fig. 6(a) to voltammetric spectra, such as breakdown voltages relative to a reference electrode, can be found in Refs. [17,98]—see also the citations therein. Promising electrolytes, which might be stable for a wide region about the "Dirac cone" in graphene or graphite could perhaps include acetonitrile and/or sulfolane [92]. Second, one can independently tune the nanodisk dimensions on each electrode to fit a given

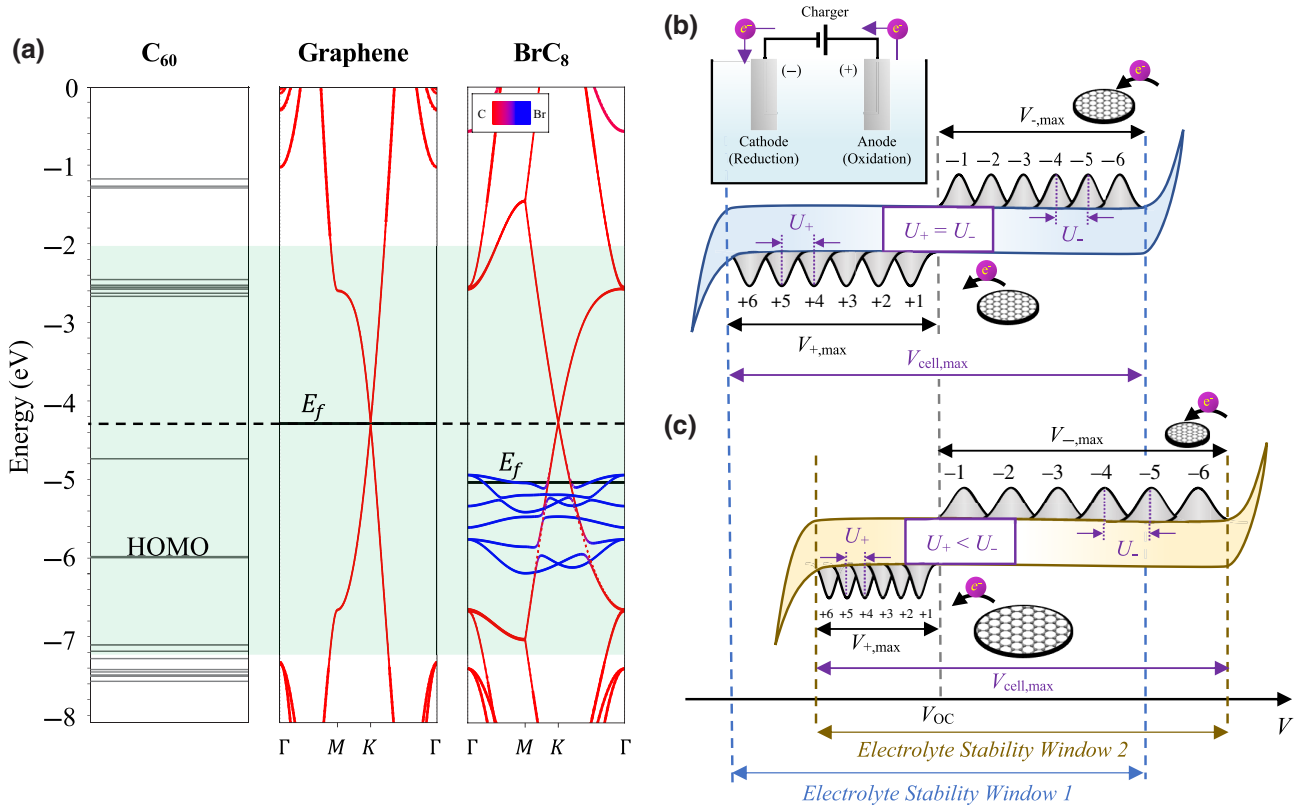

FIG. 6. (a) Comparative electronic structure plots against an electrolyte stability window (green) situated between −2 and −7 eV below vacuum. The left panel shows the electronic structure of C_{60}, the middle panel that of graphene, and the right panel that of BrC_8 decorated graphene. A dashed line provides the alignment of all electronic structure plots to the Fermi energy (E_f) of graphene. The Fermi energy of single-layer BrC_8 lies below that of graphene, due to the loss of electrons to Br atoms, but above the stability limit of the electrolyte window. (b) A schematic depicting the position of the open circuit potential (V_{OC}) within the electrolyte stability window (shaded in light blue) dictates the electrode potentials ($|V_{anode}|$ and $|V_{cathode}|$) and the maximum cell potential V_{max} for a system with symmetric electrodes. This schematic assumes the simple case that V_{OC} lies at the center of the electrolyte stability window with the equally distributed current peaks (shaded in gray) for electron removal at the positive terminal and electron addition at the negative terminal for different charge states on the graphitic nanodisks during a charging process. Here, the equal peak distribution ($U_+ = U_-$) on each terminal is achieved by nanodisks of similar radius on both sides. The inset shows the definitions of anode and cathode for a supercapacitor cell under the charging process [97]. (c) A schematic for a more frequently observed V_{OC} that lies closer to the limits for the positive electrode. To avoid wasting the wider potential window on the negative electrode, the nanodisks can be engineered to have a smaller radius for a larger U_- as compared to U_+.

electrolyte stability window alignment. This scenario is shown in Fig. 6(b), where the Dirac cone of graphite or graphene lies closer to the positive breakdown potential of the electrolyte than to its negative breakdown potential. In this case, the nanodisk radius on the positive electrode should be larger than that on the negative electrode, so as to store the same density of charge but a lower potential relative to the fully discharged configuration about the Dirac cone energy [see Fig. 6(b)]. Conversely, the nanodisks on the negative electrode can be made smaller to provide a larger voltage window for storing the same density of electrons per disk by realizing a higher charging energy cost (see Fig. 4) [29,99]. Additionally, one may overcome instability via distinct electrolytes on each terminal, as discussed in the Supplemental Material [56]. Other approaches to overcome electrolyte stability certainly exist and are left for future work [58,90,91]. Given the theoretical challenges associated with predicting electrolyte breakdown voltages, a detailed experimental investigation of quantized capacitance charging and electrolyte stability is needed to further efforts in this direction [78].

III. POWER DENSITY

The power density of conventional EDL-based supercapacitors is essentially determined by the diffusion of counterions in the charging and discharging processes [2,100–102]. When the ionic diffusion constant reaches around 10^{-10} to 10^{-9} m^2/s [103–105], these EDL-based systems can achieve high power densities of approximately 10^4 W/L (see Fig. 1). To match the power density of purely EDL-based supercapacitors as suggested by Fig. 1, a

pseudocapacitive mechanism must exhibit fast and reversible redox activity. While the reversibility of a redox system utilizing quantized capacitance is very much determined by the design considerations discussed in Sec. II D, the rate of redox activity is determined by the speed at which electrons can transfer into and out of nanoparticles, as illustrated in Fig. 2(a). Hence, there are two mechanisms that determine the power density of quantized capacitance as an energy storage medium: (1) counterion diffusion; (2) electron transfer and diffusion. Going forward we will assume that the ionic diffusion engineering issues are similar to either those of conventional EDL-based supercapacitors or organic radical batteries—leaving a detailed atomistic analysis to future work [106–108]. Instead, we focus on the manner in which the electron transfer should also be engineered to maximize the power density of this mechanism (see Fig. 1).

In order for quantized capacitance to persist, particles must be separated by a reasonable tunneling barrier. This is necessary to promote Coulombic interactions between electrons on a nanoparticle and thereby arrive at a "quantized" value of U as described by Eq. (3) [10,17]. By tuning U we are able to engineer the storage voltage for a target electron density σ_e, as discussed in Sec. II. However, this essential tunneling process cannot be so slow as to render the power density impractical (see Fig. 1). When considering the overall proposed mechanism in Fig. 2(a), the key limiting factor is the rate at which electrons are transferred between individual particles via tunneling. In the Gerischer-Hopfield description of quantized capacitance, this interparticle electron tunneling (transfer) rate can be approximated as [10,17,63,65–67,109–111]

$$k_{\mathrm{ip}} = \frac{4\pi^2|M_{\mathrm{ip}}|^2}{h}\int D_{\mathrm{red},N+1}(\varepsilon)D_{\mathrm{ox},N}(\varepsilon)d\varepsilon = \frac{4\pi^2|M_{\mathrm{ip}}|^2}{h}\frac{1}{\sqrt{4\pi\lambda_c k_B T}}\exp\left(\frac{-\lambda_c}{4k_B T}\right), \tag{9}$$

where $|M_{\mathrm{ip}}|$ is the electronic coupling between particles, h is Planck's constant, and $\lambda_c = 2\lambda$ is the classical Marcus-Hush reorganization energy. In Fig. 7(a) we can see that k_{ip} depends primarily on both $|M_{\mathrm{ip}}|$ and λ_c. The key assumption in Eq. (9) is that the electrons are weakly coupled such that the transfer mechanism is an outer-sphere (tunneling) process [62]. This intersite electron transfer mechanism is essentially the same as that present in redox-polymer batteries [60,112–114]. Now if we further assume that the nanodisks in Fig. 2(a) are uniformly spaced, such that the electronic coupling $|M_{\mathrm{ip}}|$ to all nearest-neighbor particles is approximately the same, then the diffusion of electrons in this system can be approximately written as

$$\mathcal{D}_e = \frac{l^2}{2d}k_{\mathrm{ip}}, \tag{10}$$

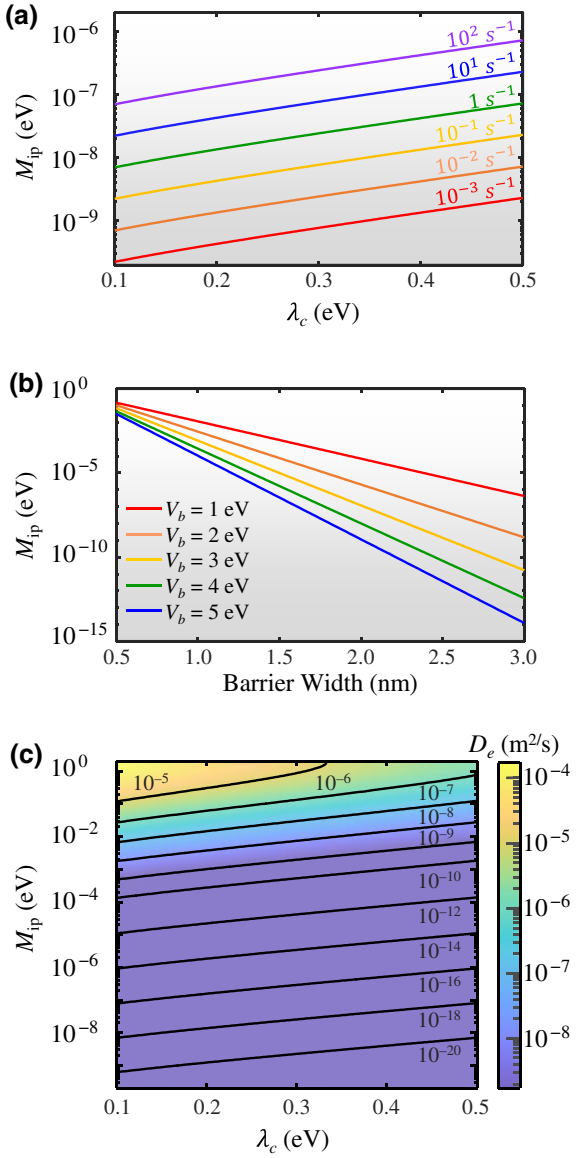

FIG. 7. (a) The $|M_{\mathrm{ip}}|$ and λ_c to achieve a specific electron transfer rate k_{ip}, ranging from 10^{-3} to 100 s^{-1}. (b) The effect of barrier width on the required M_{ip} to efficiently store the electrons at various barrier heights V_b. The value of (c) $\mathcal{D}_e$ at 300 K as a function of $|M_{\mathrm{ip}}|$ and λ_c for a 2.5 eV tunneling barrier.

where $d = 3$ is the dimensionality of the hopping process and l is the hopping distance [115]. This then allows us to rapidly arrive at an approximate understanding as to how electron diffusion should be coengineered with ionic diffusion in this system.

Assuming that the temperature is held fixed at about 300 K, the interparticle electronic coupling ($|M_{\mathrm{ip}}|$) and classical Marcus-Hush reorganization energy ($\lambda_c = 2\lambda$) primarily dominate the diffusion of electrons via Eqs. (9) and (10). To first order, the electronic coupling is further dependent upon the tunneling barrier width W and height V_b between

the particles in the manner of

$$|M_{\mathrm{ip}}| \approx 2|V_b| \exp\left(\frac{-W\sqrt{2m|V_b|}}{\hbar}\right), \tag{11}$$

which is related to the Gamow tunneling expression [116,117]—m is the electron mass and $\hbar = h/2\pi$. In Fig. 7(b) it can be seen that both the tunneling barrier height (V_b) and width (W) exponentially impact $|M_{\mathrm{ip}}|$ and thereby the electron diffusion rate ($\mathcal{D}_e$). The overall magnitude of $\mathcal{D}_e$ as a function of both $|M_{\mathrm{ip}}|$ and λ_c is plotted in Fig. 7(c). Here it can be seen that to achieve a target electron diffusion constant in the range 10^{-10}–10^{-9} m^2/s, comparable to high performance ionic diffusion, one needs to attain reorganization energies (λ_c) in the range 0.15–0.25 eV and electronic coupling strengths ($|M_{\mathrm{ip}}|$) in the range 10^{-2}–10^{-4} eV. Returning to Fig. 5(c) we can see that reorganization energies in this range should be easily achievable with $\epsilon_r > 20$. Note that these estimates do not include inner-sphere contributions to the reorganization energy, which should raise their estimate magnitudes further and impact $\mathcal{D}_e$. However, the electronic coupling range estimated may be more difficult to achieve from a practical engineering perspective.

Based on the estimates in Fig. 7(b), a tunneling barrier with a height of $V_b = 2$–3 eV and a width of about 1.2 nm would work best to provide target electron diffusion values in the range 10^{-10}–10^{-9} m^2/s [see also Fig. 7(c)]. In this system the tunneling barrier is determined by the electrolyte stability window, that is the offset between the liquid electrolyte HOMO and LUMO levels from the nanodisk levels in Eq. (7), and can be manageably engineered [118,119]. The requirement for maintaining an interdisk separation of about 1.2 nm is much more difficult to implement, as it is directly coupled to the volumetric packing of such nanodisks, as discussed earlier in the context of Fig. 3. This somewhat stringent spacing criteria, which excludes any randomness in packing, could likely be alleviated by introducing electron shuttling sites such as buckyballs [120–122]. Such species could act as intermediate transfer centres to carry electrons between nanodisks that are separated by more than about 1.2 nm, due to packing randomness, and thereby prevent the effective electronic coupling between nanodisks from becoming too low. Interestingly, an interdisk spacing corresponding to about 1.2 nm could also aid the diffusion of counterions by possibly removing the traditional solvation shell limitations [123–125]. From this perspective, our theoretical estimates for optimum packing to promote electron diffusion may also similarly aid counterion diffusion. Here, it is important to realize that both electron diffusion and ion diffusion can impact the power density of a pseudocapacitive battery operating via quantized capacitance. This aligns with the findings reported in Refs. [114,126], where the concerted diffusion of ions and electrons are shown to impact energy performance. However, a conclusive exploration of these issues requires detailed atomistic calculations coupled with careful experimentation [106,108,127–130].

IV. DISCUSSION AND CONCLUSION

Before concluding, it is helpful to consider existing technological reference points through which this energy storage design might be better understood. As briefly mentioned in Sec. I, redox-polymer batteries are perhaps the most relevant practical analogue to the system explored herein (see Fig. 2) [22,131]. In both designs redox centres are dispersed in a supporting medium, with operation facilitated by the classical diffusion of counterions and the tunneling (outer-sphere transfer) diffusion of electrons [126]. Unlike redox-polymer batteries, quantized capacitance is capable of producing multiple redox reactions on a single site, in such a manner that the Faradaic current is able to mimic a pseudocapacitive response, as shown in Fig. 4 [10,17,54]. In a sense one could think of the proposed mechanism as a "pseudocapacitive battery"—though quantized capacitance is not limited to carbon-based nanoparticles [11–16]. Clearly, the physical distinction between a pseudocapacitive Faradaic mechanism and that of a battery begins to blur in this domain.

Overall, reliable synthesis likely remains the major obstacle to prototyping quantized capacitance as a storage mechanism—though electrolyte stability should not be ignored, as discussed in Sec. II D. Firstly, one should be able to produce low variability in the synthesized dimensions of nanoparticles. This is needed to ensure that the nanoparticle charging energy is tailored to store a desired electron density at or near a target voltage, as discussed in Sec. II C. Though certainly some degree of tolerance in synthesis size within an ensemble should be acceptable [16,32]. Secondly, the requirement that they be singly packed and separated by reasonably well-controlled tunneling barriers could be difficult to fabricate—particularly at a large scale. Nevertheless though, cumulative engineering development quantum dots have been integrated into large-scale fabrication processes [132–134]. With impetus, similar engineering advances might make the quantized capacitance scheme in Fig. 2(a) more practically tangible. For example, it has recently been shown that the interplanar distance of graphene oxide can be finely tuned [23,24], thereby demonstrating the possibility to precisely control the interparticle distance in supercapacitor systems. Additionally, carbon nanotubes of uniform structure and dimensionality can now be routinely fabricated [135–137]. Similar approaches might be applied to make this theoretically benchmarked system a realizable "pseudocapacitive battery" technology.

There is also a possibility of combining the proposed quantized capacitance setup within other emerging EDL technologies. For example, rather than utilizing the single

electrode setup in Fig. 2(a), a matrix of nanodisks could be imbedded between stacked MXenes sheets [138–140]. The nanodisk matrix would add a Faradaic storage component to such a supercapacitor system. Likewise, vertically aligned MXene layers would also aid fast ionic diffusion. In this manner, two such technologies might complement each other to improve overall performance (see the Supplemental Material [56]). Similar hybrid approaches could be applied with other supercapacitor systems [38,40,141]. Even a slurry-type redox flow battery utilizing quantized capacitance to access multiple redox states is plausible [41–43].

Returning to the Ragone plot in Fig. 1, all of the theoretical analysis conducted herein suggests that quantized capacitance might be engineered to combine the power performance of supercapacitors with the energy density of battery systems. Theoretically, quantized capacitance could yield an energy density of 100 Wh/L combined with a power density of 10^4 W/L. This would be a tangible benchmark worth pursuing in the development of this mechanism [21,142,143], and further exploring system-specific engineering parameters in more detailed studies. However, in our analysis we have omitted the gravimetric energy density, instead focusing on the volumetric density. This is a key point to consider and relies entirely on the materials utilized to construct such a system, with the number of chemical permutations being vast. Optimistically, a primarily carbon-based system [as illustrated in Fig. 2(a)] would offer a high gravimetric density. However, the choice of counterions also plays a critical role in determining the gravimetric density [144–146]. Going forward, close collaboration between theory and experiment are needed to resolve and analyze specific systems with the aim of fabricating such a "pseudocapacitive battery" capable of the theoretical limits outlined herein. Future work should focus on experimentally benchmarking specific systems through state-of-the-art characterization coupled with sophisticated atomistic calculations [39,147,148].

ACKNOWLEDGMENTS

All authors gratefully acknowledge financial support from the Natural Sciences & Engineering Research Council of Canada. Computational resources were provided by the Canadian Foundation for Innovation, CalculQuebec and Compute-Canada. The authors would like to acknowledge financial support from EPSRC Grant No. EP/R034540/1 for the JSPS-EPSRC-McGill University collaboration on "Defect Functionalized Sustainable Energy Materials: From Design to Devices Application" and UCL for travel support.

Y.W.F. conducted the analysis, benchmarking, and electrolyte optimization content. K.H.B. developed the formalism and energy storage concept. C.A.H. contributed the electron removal and electrolyte stability concepts and analysis associated with carbon nanostructures. The first-principles calculations were conducted by J.S. and S.Y. under the supervision of K.H.B. All of the authors discussed the results and participated in composing the manuscript.

[1] Z.-S. Wu, K. Parvez, X. Feng, and K. Müllen, Graphene-based in-plane micro-supercapacitors with high power and energy densities, Nat. Commun. **4**, 2487 (2013).

[2] S. Fleischmann, Y. Zhang, X. Wang, P. T. Cummings, J. Wu, P. Simon, Y. Gogotsi, V. Presser, and V. Augustyn, Continuous transition from double-layer to Faradaic charge storage in confined electrolytes, Nat. Energy **7**, 222 (2022).

[3] P. Li, T. Shang, X. Dong, H. Li, Y. Tao, and Q. H. Yang, A review of compact carbon design for supercapacitors with high volumetric performance, Small (Weinheim an der Bergstrasse, Germany) **17**, e2007548 (2021).

[4] E. Pomerantseva, F. Bonaccorso, X. Feng, Y. Cui, and Y. Gogotsi, Energy storage: The future enabled by nanomaterials, Science **366**, eaan8285 (2019).

[5] M. K. Jha and C. Subramaniam, Design principles for manipulating electrochemical interfaces in solid-state supercapacitors for wearable applications, ACS Omega **6**, 7970 (2021).

[6] J. P. Mensing, T. Lomas, and A. Tuantranont, 2D and 3D printing for graphene based supercapacitors and batteries: A review, Sustain. Mater. Technol. **25**, e00190 (2020).

[7] P. Iamprasertkun, W. Hirunpinyopas, A. Keerthi, B. Wang, B. Radha, M. A. Bissett, and R. A. W. Dryfe, Capacitance of basal plane and edge-oriented highly ordered pyrolytic graphite: Specific ion effects, J. Phys. Chem. Lett. **10**, 617 (2019).

[8] C. Zhan, M. Naguib, M. Lukatskaya, P. R. C. Kent, Y. Gogotsi, and D.-e. Jiang, Understanding the MXene pseudocapacitance, J. Phys. Chem. Lett. **9**, 1223 (2018).

[9] K. A. Stoerzinger, R. R. Rao, X. R. Wang, W. T. Hong, C. M. Rouleau, and Y. Shao-Horn, The role of Ru redox in pH-dependent oxygen evolution on rutile ruthenium dioxide surfaces, Chem **2**, 668 (2017).

[10] Y. W. Foong, M. S. Hossain, S. V. Sukhomlinov, and K. H. Bevan, Faradaic quantized capacitance as an ideal pseudocapacitive mechanism, J. Phys. Chem. C **125**, 4343 (2021).

[11] D. T. Miles and R. W. Murray, Temperature-dependent quantized double layer charging of monolayer-protected gold clusters, Anal. Chem. **75**, 1251 (2003).

[12] J. F. Hicks, D. T. Miles, and R. W. Murray, Quantized double-layer charging of highly monodisperse metal nanoparticles, J. Am. Chem. Soc. **124**, 13322 (2002).

[13] S. Chen and R. W. Murray, Electrochemical quantized capacitance charging of surface ensembles of gold nanoparticles, J. Phys. Chem. B **103**, 9996 (1999).

[14] J. F. Hicks, A. C. Templeton, S. Chen, K. M. Sheran, R. Jasti, R. W. Murray, J. Debord, T. G. Schaaff, and R. L. Whetten, The monolayer thickness dependence of quantized double-layer capacitances of monolayer-protected gold clusters, Anal. Chem. **71**, 3703 (1999).

[15] J. J. Pietron, J. F. Hicks, and R. W. Murray, Using electrons stored on quantized capacitors in electron transfer reactions, J. Am. Chem. Soc. **121**, 5565 (1999).

[16] S. Chen, R. W. Murray, and S. W. Feldberg, Quantized capacitance charging of monolayer-protected Au clusters, J. Phys. Chem. B **102**, 9898 (1998).

[17] K. H. Bevan, Y. W. Foong, J. Shirani, S. Yuan, and S. Abi Farraj, Physics applied to electrochemistry: Tunneling reactions, Int. J. Appl. Phys. **129**, 090901 (2021).

[18] P. Sharma and V. Kumar, Current technology of supercapacitors: A review, J. Electron. Mater. **49**, 3520 (2020).

[19] Poonam, K. Sharma, A. Arora, and S. K. Tripathi, Review of supercapacitors: Materials and devices, J. Energy Storage **21**, 801 (2019).

[20] M. K. Shobana, Self-supported materials for battery technology - a review, J. Alloys Compd. **831**, 154844 (2020).

[21] W. Zuo, R. Li, C. Zhou, Y. Li, J. Xia, and J. Liu, Battery-supercapacitor hybrid devices: Recent progress and future prospects, Adv. Sci. **4**, 1600539 (2017).

[22] H. Nishide and T. Suga, Organic radical battery, Electrochem. Soc. Interface **14**, 32 (2005).

[23] A. J. Clancy, M. K. Bayazit, S. A. Hodge, N. T. Skipper, C. A. Howard, and M. S. P. Shaffer, Charged carbon nanomaterials: Redox chemistries of fullerenes, carbon nanotubes, and graphenes, Chem. Rev. **118**, 7363 (2018).

[24] Z. Li, S. Gadipelli, H. Li, C. A. Howard, D. J. L. Brett, P. R. Shearing, Z. Guo, I. P. Parkin, and F. Li, Tuning the interlayer spacing of graphene laminate films for efficient pore utilization towards compact capacitive energy storage, Nat. Energy **5**, 160 (2020).

[25] L. Echegoyen and L. E. Echegoyen, Electrochemistry of fullerenes and their derivatives, Acc. Chem. Res. **31**, 593 (1998).

[26] K. Ji, J. Han, A. Hirata, T. Fujita, Y. Shen, S. Ning, P. Liu, H. Kashani, Y. Tian, Y. Ito, J.-i. Fujita, and Y. Oyama, Lithium intercalation into bilayer graphene, Nat. Commun. **10**, 1 (2019).

[27] C. Wang, S. Zhai, Z. Yuan, J. Chen, X. Zhang, Q. Huang, Y. Wang, X. Liao, L. Wei, and Y. Chen, A core-sheath holey graphene/graphite composite fiber intercalated with MoS_2 nanosheets for high-performance fiber supercapacitors, Electrochim. Acta **305**, 493 (2019).

[28] Z. Zhang, J. Zhao, C. Guo, and J. Xu, Intercalation pseudocapacitance of expanded graphite in sodium-ion capacitors, Micro Nano Lett. **13**, 669 (2018).

[29] D. B. Shinde and V. K. Pillai, Electrochemical resolution of multiple redox events for graphene quantum dots, Angew. Chem. Int. Ed. **52**, 2482 (2013).

[30] A. Roy-Gobeil, Y. Miyahara, K. H. Bevan, and P. Grutter, Fully quantized electron transfer observed in a single redox molecule at a metal interface, Nano Lett. **19**, 6104 (2019).

[31] S. Chen, R. S. Ingram, M. J. Hostetler, J. J. Pietron, R. W. Murray, T. G. Schaaff, J. T. Khoury, M. M. Alvarez, and R. L. Whetten, Gold nanoelectrodes of varied size: Transition to molecule-like charging, Science **280**, 2098 (1998).

[32] R. Sardar, A. M. Funston, P. Mulvaney, and R. W. Murray, Gold nanoparticles: Past, present, and future, Langmuir **25**, 13840 (2009).

[33] T. Yatsuhashi and N. Nakashima, Multiple ionization and Coulomb explosion of molecules, molecular complexes, clusters and solid surfaces, J. Photochem. Photobiol. C: Photochem. Rev. **34**, 52 (2018).

[34] A. A. Kornyshev, Double-layer in ionic liquids: Paradigm change?, J. Phys. Chem. B **111**, 5545 (2007).

[35] T. Janoschka, M. D. Hager, and U. S. Schubert, Powering up the future: Radical polymers for battery applications, Adv. Mater. **24**, 6397 (2012).

[36] M. D. Hager, B. Esser, X. Feng, W. Schuhmann, P. Theato, and U. S. Schubert, Polymer-based batteries—flexible and thin energy storage systems, Adv. Mater. **32**, 2000587 (2020).

[37] M. Stolar, Organic electrochromic molecules: Synthesis, properties, applications and impact, Pure Appl. Chem. **92**, 717 (2020).

[38] S. A. Melchior, K. Raju, I. S. Ike, R. M. Erasmus, G. Kabongo, I. Sigalas, S. E. Iyuke, and K. I. Ozoemena, High-voltage symmetric supercapacitor based on 2D titanium carbide (MXene, Ti_2CT_x/carbon nanosphere composites in a neutral aqueous electrolyte, J. Electrochem. Soc. **165**, A501 (2018).

[39] Y. Dong, Z. Tang, P. Liang, H. Wan, H. Wang, L. Wang, H. Shu, and D. Chao, 2D-VN_2 MXene as a novel anode material for Li, Na and K ion batteries: Insights from the first-principles calculations, J. Colloid Interface Sci. **593**, 51 (2021).

[40] Y. Yoon, M. Lee, S. K. Kim, G. Bae, W. Song, S. Myung, J. Lim, S. S. Lee, T. Zyung, and K.-S. An, A strategy for synthesis of carbon nitride induced chemically doped 2D MXene for high-performance supercapacitor electrodes, Adv. Energy Mater. **8**, 1703173 (2018).

[41] J. Montero, P. Navalpotro, A. ĎEpifanio, B. Mecheri, S. Licoccia, and J. Carretero-González, Redox-active coordination polymers as bifunctional electrolytes in slurry-based aqueous batteries at neutral pH, J. Electroanal. Chem. **895**, 115442 (2021).

[42] J. Lohaus, D. Rall, M. Kruse, V. Steinberger, and M. Wessling, On charge percolation in slurry electrodes used in vanadium redox flow batteries, Electrochem. Commun. **101**, 104 (2019).

[43] W. Yan, C. Wang, J. Tian, G. Zhu, L. Ma, Y. Wang, R. Chen, Y. Hu, L. Wang, T. Chen, J. Ma, and Z. Jin, All-polymer particulate slurry batteries, Nat. Commun. **10**, 2513 (2019).

[44] Q. Wang and W. A. Daoud, Aqueous multi-electron electrolyte for hybrid flow batteries with high energy and power densities, J. Power Sources **4**, 100018 (2020).

[45] B. E. Conway, *Electrochemical Supercapacitors: Scientific Fundamentals and Technological Applications* (Plenum Press, New York, 1999).

[46] D. Sergeyev, N. Ashikov, and N. Zhanturina, Electric transport properties of a model nanojunction "graphene-fullerene C_{60}-graphene", Int. J. Nanosci. **20**, 2150007 (2020).

[47] D. Gao, S. M. Aly, P. L. Karsenti, G. Brisard, and P. D. Harvey, Application of the boron center for the design of a covalently bonded closely spaced triad of porphyrin-fullerene mediated by dipyrromethane, Dalton Trans. (Cambridge, England : 2003) **46**, 6278 (2017).

[48] C. Chua, A. Lartsev, J. Sui, V. Panchal, R. Puddy, C. Richardson, C. G. Smith, T. J. B. M. Janssen, A. Tzalenchuk, R. Yakimova, S. Kubatkin, and M. R. Connolly, Observation of coulomb blockade in nanostructured epitaxial bilayer graphene on SiC, Carbon **119**, 426 (2017).

[49] Z. Tan, G. Liu, L. Lu, and C. Yang, Observation of Coulomb blockade and ballistic tunneling in graphene single electron transistor, Sci. China: Phys. Mech. Astron. **55**, 7 (2012).

[50] S. Choi, G. Jung, J. E. Kim, T. Kim, and K. S. Suh, Lithium intercalated graphite with preformed passivation layer as superior anode for lithium ion batteries, Appl. Surf. Sci. **455**, 367 (2018).

[51] H. Fan, L. Qi, and H. Wang, Hexafluorophosphate anion intercalation into graphite electrode from methyl propionate, Solid State Ion **300**, 169 (2017).

[52] Y. Huang, L. Qi, and H. Wang, Intercalation of anions into graphite electrode from butylene carbonate in activated carbon/graphite hybrid capacitors, Electrochim. Acta **258**, 380 (2017).

[53] K. H. Bevan, M. S. Hossain, A. Iqbal, and Z. Wang, Exploring bridges between quantum transport and electrochemistry. I, J. Phys. Chem. C **120**, 179 (2016).

[54] M. S. Hossain, B. Muralidharan, and K. H. Bevan, A general theoretical framework for characterizing solvated electronic structure via voltammetry: Applied to carbon nanotubes, J. Phys. Chem. C **121**, 18288 (2017).

[55] M. R. Zoric, V. Singh, S. Warren, S. Plunkett, R. R. Khatmullin, B. P. Chaplin, and K. D. Glusac, Electron transfer kinetics at graphene quantum dot assembly electrodes, ACS Appl. Mater. Interfaces **11**, 46303 (2019).

[56] See Supplemental Material at http://link.aps.org/supplemental/10.1103/PRXEnergy.1.013007 for energy density calculations; for the potential calculation on a nanodisk, which includes Refs. [149,150]; for first-principles calculations of the energy levels, which includes Refs. [151–164]; for the engineering approach with two electrolytes to overcome the electrolyte stability window limitations, which also includes Refs. [165–175]; and for the design approach using MXene layers.

[57] X. Tian, Q. Zhu, and B. Xu, "Water-in-salt" electrolytes for supercapacitors: A review, ChemSusChem **14**, 2501 (2021).

[58] A. Virya and K. Lian, A review of neutral pH polymer electrolytes for electrochemical capacitors: Transitioning from liquid to solid devices, Materials Reports: Energy **1**, 100005 (2021).

[59] L. Yin, S. Li, X. Liu, and T. Yan, Ionic liquid electrolytes in electric double layer capacitors, Sci. China Mater. **62**, 1537 (2019).

[60] H. Chen, G. Cong, and Y.-C. Lu, Recent progress in organic redox flow batteries: Active materials, electrolytes and membranes, J. Energy Chem. **27**, 1304 (2018).

[61] O. Ciftja and I. Hysi, The electrostatic potential of a uniformly charged disk as the source of novel mathematical identities, Appl. Math. Lett. **24**, 1919 (2011).

[62] K. H. Bevan, Electron transfer from the perspective of electron transmission: Biased non-adiabatic intermolecular reactions in the single-particle picture, J. Chem. Phys. **146**, 134106 (2017).

[63] J. J. Hopfield, Electron transfer between biological molecules by thermally activated tunneling, Proc. Natl. Acad. Sci. USA **71**, 3640 (1974).

[64] V. R. Jupally, J. G. Thrasher, and A. Dass, Quantized double layer charging of $Au_{130}(SR)_{50}$ nanomolecules, Analyst **139**, 1826 (2014).

[65] H. Gerischer, Über den ablauf von redoxreaktionen an metallen und an halbleitern, Z. Phys. Chem. **26**, 325 (1960).

[66] H. Gerischer, Über den ablauf von redoxreaktionen an metallen und an halbleitern, Z. Phys. Chem. **26**, 223 (1960).

[67] H. Gerischer, Über den ablauf von redoxreaktionen an metallen und an halbleitern, Z. Phys. Chem. **27**, 48 (1961).

[68] S. Park and J. G. McDaniel, Interference of electrical double layers: Confinement effects on structure, dynamics, and screening of ionic liquids, J. Chem. Phys. **152**, 074709 (2020).

[69] M. S. Hossain, A. Iqbal, and K. H. Bevan, Interfacial screening in ultrafast voltammetry: A theoretical study of redox-active monolayers, Anal. Chem. **88**, 9062 (2016).

[70] G. Feng and P. T. Cummings, Supercapacitor capacitance exhibits oscillatory behavior as a function of nanopore size, J. Phys. Chem. Lett. **2**, 2859 (2011).

[71] D.-e. Jiang, Z. Jin, and J. Wu, Oscillation of capacitance inside nanopores, Nano Lett. **11**, 5373 (2011).

[72] G. Feng, R. Qiao, J. Huang, B. G. Sumpter, and V. Meunier, Ion distribution in electrified micropores and its role in the anomalous enhancement of capacitance, ACS Nano **4**, 2382 (2010).

[73] Y. Liu, Y. Bai, W. Jaegermann, R. Hausbrand, and B. X. Xu, Impedance modeling of solid-state electrolytes: Influence of the contacted space charge layer, ACS Appl. Mater. Interfaces **13**, 5895 (2021).

[74] C. G. J. Baker and E. R. Buckle, Double layer relaxation in liquid electrolytes. Part 1.—Theory of the space charge polarization, Trans. Faraday Soc. **64**, 469 (1968).

[75] A. J. Clancy, M. K. Bayazit, S. A. Hodge, N. T. Skipper, C. A. Howard, and M. S. P. Shaffer, Charged carbon nanomaterials: Redox chemistries of fullerenes, carbon nanotubes, and graphenes, Chem. Rev. **118**, 7363 (2018).

[76] C. A. Howard, J. C. Wasse, N. T. Skipper, H. Thompson, and A. K. Soper, The solvation structure of fulleride C_{60}^{5-} anions in potassium ammonia solution, J. Phys. Chem. C **111**, 5640 (2007).

[77] C. A. Howard, H. Thompson, J. C. Wasse, and N. T. Skipper, Formation of giant solvation shells around fulleride anions in liquid ammonia, J. Am. Chem. Soc. **126**, 13228 (2004).

[78] C. Bruno, I. Doubitski, M. Marcaccio, F. Paolucci, D. Paolucci, and A. Zaopo, Electrochemical generation of C_{60}^{2+} and C_{60}^{3+}, J. Am. Chem. Soc. **125**, 15738 (2003).

[79] C. Stampfer, J. Guttinger, F. Molitor, D. Graf, T. Ihn, and K. Ensslin, Tunable Coulomb blockade in nanostructured graphene, Appl. Phys. Lett. **92**, 12102 (2008).

[80] D. K. Böhme, Fullerene ion chemistry: A journey of discovery and achievement, Philos. Trans. R. Soc. A **374**, 20150321 (2016).

[81] S. Petrie and D. K. Bohme, Gas-phase association reactions of fullerene cations: Modelling the influence of

charge state and other molecular parameters on association efficiency, Can. J. Chem. **72**, 577 (1994).
[82] D. A. Young, The intercalation process in graphite-bromine, Carbon **15**, 373 (1977).
[83] W. Zhao, P. H. Tan, J. Liu, and A. C. Ferrari, Intercalation of few-layer graphite flakes with $FeCl_3$: Raman determination of Fermi level, layer by layer decoupling, and stability, J. Am. Chem. Soc. **133**, 5941 (2011).
[84] M. S. Hossain and K. H. Bevan, Exploring bridges between quantum transport and electrochemistry. II. A theoretical study of redox-active monolayers, J. Phys. Chem. C **120**, 188 (2016).
[85] *CRC Handbook of Chemistry and Physics*, 88th ed. (CRC Press, 2007).
[86] M. Kim, M. C. Tringides, M. T. Hershberger, S. Chen, M. Hupalo, P. A. Thiel, C.-Z. Wang, and K.-M. Ho, Manipulation of Dirac cones in intercalated epitaxial graphene, Carbon **123**, 93 (2017).
[87] T. T. Jia, M. M. Zheng, X. Y. Fan, Y. Su, S. J. Li, H. Y. Liu, G. Chen, and Y. Kawazoe, Dirac cone move and bandgap on/off switching of graphene superlattice, Sci. Rep. **6**, 18869 (2016).
[88] S. Pisana, M. Lazzeri, C. Casiraghi, K. S. Novoselov, A. K. Geim, A. C. Ferrari, and F. Mauri, Breakdown of the adiabatic Born-Oppenheimer approximation in graphene, Nat. Mater. **6**, 198 (2007).
[89] C. A. Howard, M. P. M. Dean, and F. Withers, Phonons in potassium-doped graphene: The effects of electron-phonon interactions, dimensionality, and adatom ordering, Phys. Rev. B **84**, 241404 (2011).
[90] P. Raghavan and M. J. Jabeen Fatima, *Polymer Electrolytes for Energy Storage Devices* (CRC Press, Boca Raton, 2021), 1st ed.
[91] S. Alipoori, S. Mazinani, S. H. Aboutalebi, and F. Sharif, Review of PVA-based gel polymer electrolytes in flexible solid-state supercapacitors: Opportunities and challenges, J. Energy Storage **27**, 101072 (2020).
[92] E. L. Bennett, C. Song, Y. Huang, and J. Xiao, Measured relative complex permittivities for multiple series of ionic liquids, J. Mol. Liq. **294**, 111571 (2019).
[93] G. Profeta, M. Calandra, and F. Mauri, Phonon-mediated superconductivity in graphene by lithium deposition, Nat. Phys. **8**, 131 (2012).
[94] S.-L. Yang, J. A. Sobota, C. A. Howard, C. J. Pickard, M. Hashimoto, D. H. Lu, S.-K. Mo, P. S. Kirchmann, and Z.-X. Shen, Superconducting graphene sheets in CaC_6 enabled by phonon-mediated interband interactions, Nat. Commun. **5**, 3493 (2014).
[95] Z.-H. Pan, J. Camacho, M. H. Upton, A. V. Fedorov, C. A. Howard, M. Ellerby, and T. Valla, Electronic Structure of Superconducting KC_8 and Nonsuperconducting LiC_6 Graphite Intercalation Compounds: Evidence for a Graphene-Sheet-Driven Superconducting State, Phys. Rev. Lett. **106**, 187002 (2011).
[96] T. F. Fuller and J. N. Harb, *Electrochemical Engineering* (Wiley, Hoboken, NJ, USA, 2018), 1st ed.
[97] S. Adams, G. B. Appetechi, M. V. Avdeev, P. B. Balbuena, H. Bardt, E. Berendes, V. A. Blatov, I. Bobrikov, L. G. Bulusheva, and P. Canepa, *Electrochemical Storage Materials: From Crystallography to Manufacturing Technology*, edited by D. C. Meyer, T. Leisegang, M. Zschornak, and H. Stöcker (Walter de Gruyter GmbH and Co KG, 2018).
[98] T. J. Smith, K. J. Stevenson, and C. G. Zoski, in *Handbook of Electrochemistry* (Elsevier, Amsterdam, 2007), p. 73.
[99] J. Li, P. Song, J. Zhao, K. Vaklinova, X. Zhao, Z. Li, Z. Qiu, Z. Wang, L. Lin, M. Zhao *et al.*, Printable two-dimensional superconducting monolayers, Nat. Mater. **20**, 181 (2021).
[100] A. Forse, J. Griffin, C. Merlet, J. Carretero-Gonzalez, A.-R. Raji, N. Trease, and C. Grey, Direct observation of ion dynamics in supercapacitor electrodes using in situ diffusion NMR spectroscopy, Nat. Energy **2**, 16216 (2017).
[101] K. Breitsprecher, C. Holm, and S. Kondrat, Charge me slowly, I am in a hurry: Optimizing charge-discharge cycles in nanoporous supercapacitors, ACS Nano **12**, 9733 (2018).
[102] R. Burt, K. Breitsprecher, B. Daffos, P.-L. Taberna, P. Simon, G. Birkett, X. S. Zhao, C. Holm, and M. Salanne, Capacitance of nanoporous carbon-based supercapacitors is a trade-off between the concentration and the separability of the ions, J. Phys. Chem. Lett. **7**, 4015 (2016).
[103] P. Banerjee and B. Bagchi, Ions' motion in water, J. Chem. Phys. **150**, 190901 (2019).
[104] R. Dubey and V. Guruviah, Review of carbon-based electrode materials for supercapacitor energy storage, Ionics **25**, 1419 (2019).
[105] G. A. Bozhikov, G. D. Bontchev, P. I. Ivanov, A. N. Priemyshev, O. D. Maslov, M. V. Milanov, and S. N. Dmitriev, Electrophoretic method for the determination of diffusion coefficients of ions in aqueous solutions, J. Radioanal. Nucl. Chem. **258**, 645 (2003).
[106] Y. Zhang, B. Dyatkin, and P. T. Cummings, Molecular investigation of oxidized graphene: Anatomy of the double-layer structure and ion dynamics, J. Phys. Chem. C **123**, 12583 (2019).
[107] W. R. Fawcett, Monte Carlo studies of ion size effects in the diffuse double layer, Electrochim. Acta **54**, 4997 (2009).
[108] E. Spohr, Molecular dynamics simulations of water and ion dynamics in the electrochemical double layer, Solid State Ion. **150**, 1 (2002).
[109] W. Schmickler, *Interfacial Electrochemistry* (Oxford University Press, 1996), 1st ed.
[110] A. J. Bard and L. R. Faulkner, *Electrochemical Methods: Fundamentals and Applications* (Wiley, New York, 2001), 2nd ed.
[111] C. E. D. Chidsey, Free energy and temperature dependence of electron transfer at the metal-electrolyte interface, Science **251**, 919 (1991).
[112] C. Friebe and U. S. Schubert, High-power-density organic radical batteries, Top Curr Chem. **375**, 1 (2017).
[113] N. Dardenne, X. Blase, G. Hautier, J.-C. Charlier, and G.-M. Rignanese, Ab initio calculations of open-cell voltage in Li-ion organic radical batteries, J. Phys. Chem. C **119**, 23373 (2015).
[114] S. N. Kerisit, K. M. Rosso, Z. Yang, and J. Liu, W. A. U. S. Pacific Northwest National Lab. (PNNL), Richland, Dynamics of coupled lithium/electron diffusion in TiO_2 polymorphs, J. Phys. Chem. C **113**, 20998 (2009).

[115] Z. Wang and K. H. Bevan, Exploring the impact of semi-core level electronic relaxation on polaron dynamics: An adiabatic *ab initio* study of $FePO_4$, Phys. Rev. B Condens. Matter **93**, 024303 (2016).

[116] D. J. Griffiths, *Introduction to Quantum Mechanics* (Pearson Prentice Hall, Upper Saddle River, NJ, 2005), 2nd ed.

[117] G. Gamow, Zur quantentheorie des atomkernes, Z. Phys. **51**, 204 (1928).

[118] K. H. Bevan, S. Datta, D. Kienle, and H. Guo, First-principles nonequilibrium analysis of STM-induced molecular negative-differential resistance on Si(100), Phys. Rev. B Condens. Matter Mater. Phys. **78**, 035303 (2008).

[119] S. Datta, W. Tian, S. Hong, R. Reifenberger, J. I. Henderson, and C. P. Kubiak, Current-Voltage Characteristics of Self-Assembled Monolayers by Scanning Tunneling Microscopy, Phys. Rev. Lett. **79**, 2530 (1997).

[120] Y. Kuang, C. Chen, D. Kirsch, and L. Hu, Thick electrode batteries: Principles, opportunities, and challenges, Adv. Energy Mater. **9**, 1901457 (2019).

[121] J. Friedl, M. A. Lebedeva, K. Porfyrakis, U. Stimming, and T. W. Chamberlain, All-fullerene-based cells for non-aqueous redox flow batteries, J. Am. Chem. Soc. **140**, 401 (2018).

[122] C. N. Sun, T. A. J. Zawodzinski, W. E. Tenhaeff, F. Ren, J. K. Keum, S. Bi, D. Li, S. K. Ahn, K. Hong, A. J. Rondinone, J. M. Carrillo, C. Do, B. G. Sumpter, and J. Chen, Nanostructure enhanced ionic transport in fullerene reinforced solid polymer electrolytes, Phys. Chem. Chem. Phys. **17**, 8266 (2015).

[123] C. Young, T. Park, J. W. Yi, J. Kim, M. S. A. Hossain, Y. V. Kaneti, and Y. Yamauchi, Advanced functional carbons and their hybrid nanoarchitectures towards supercapacitor applications, ChemSusChem **11**, 3546 (2018).

[124] Z. Wu, L. Li, J.-m. Yan, and X.-b. Zhang, Materials design and system construction for conventional and new-concept supercapacitors, Adv. Sci. **4**, 1600382 (2017).

[125] J. Zhi, Y. Wang, S. Deng, and A. Hu, Study on the relation between pore size and supercapacitance in mesoporous carbon electrodes with silica-supported carbon nanomembranes, RSC Adv. **4**, 40296 (2014).

[126] T. W. Kemper, R. E. Larsen, and T. Gennett, Relationship between molecular structure and electron transfer in a polymeric nitroxyl-radical energy storage material, J. Phys. Chem. C **118**, 17213 (2014).

[127] M. M. Islam and T. Ohsaka, Model of electrical double layer structure at semi-metallic electrode/ionic liquid interface, Electrochim. Acta **368**, 137555 (2021).

[128] P.-Y. Yang, S.-P. Ju, H.-S. Hsieh, J.-S. Lin, and J.-Y. Hsieh, Electrolytic molecule in-pore structure and capacitance of supercapacitors with nanoporous carbon electrodes: A coarse-grained molecular dynamics study, Comput. Mater. Sci. **166**, 293 (2019).

[129] O. E. Dagdeviren, A. Mascaro, S. Yuan, J. Shirani, K. H. Bevan, and P. Grutter, Ergodic and nonergodic dynamics of oxygen vacancy migration at the nanoscale in inorganic perovskites, Nano Lett. **20**, 7530 (2020).

[130] A. Mascaro, Z. Wang, P. Hovington, Y. Miyahara, A. Paolella, V. Gariepy, Z. Feng, T. Enright, C. Aiken, and K. Zaghib, Measuring spatially resolved collective ionic transport on lithium battery cathodes using atomic force microscopy, Nano Lett. **17**, 4489 (2017).

[131] E. P. Tomlinson, M. E. Hay, and B. W. Boudouris, Radical polymers and their application to organic electronic devices, Macromolecules **47**, 6145 (2014).

[132] Y.-H. Ko, P. Prabhakaran, S. Choi, G.-J. Kim, C. Lee, and K.-S. Lee, Environmentally friendly quantum-dot color filters for ultra-high-definition liquid crystal displays, Sci. Rep. **10**, 15817 (2020).

[133] L. Chen, S. Zhang, M. Zhou, X. Zhang, Z. Song, Y. Hou, X. Lin, J. Zhao, X. W. Sun, and S. C. A. Lien, A quantum dot polarizer for liquid crystal displays with much improved efficiency and viewing angle, IEEE J. Quantum Electron. **55**, 1 (2019).

[134] Y. Liu, J. Lai, X. Li, Y. Xiang, J. Li, and J. Zhou, A quantum dot array for enhanced tricolor liquid-crystal display, IEEE Photonics J. **9**, 6900207 (2017).

[135] K. Xia, H. Zhan, and Y. Gu, Graphene and carbon nanotube hybrid structure: A review, Procedia IUTAM **21**, 94 (2017).

[136] H. Rokadia, M. Gordon, and S. Tung, Carbon nanotube alignment using dielectrophoresis: A design guideline for realizing future multiwalled carbon nanotube-based devices, IEEE Nanotechnol. Mag. **10**, 24 (2016).

[137] Y. Segawa, A. Yagi, K. Matsui, and K. Itami, Design and synthesis of carbon nanotube segments, Angew. Chem. Int. Ed. **55**, 5136 (2016).

[138] J. Li, X. Wang, W. Sun, K. Maleski, C. E. Shuck, K. Li, P. Urbankowski, K. Hantanasirisakul, X. Wang, P. Kent, H. Wang, and Y. Gogotsi, Intercalation-induced reversible electrochromic behavior of two-dimensional $Ti_3C_2T_x$ MXene in organic electrolytes, ChemElectroChem **8**, 151 (2021).

[139] Q. Jiang, N. Kurra, M. Alhabeb, Y. Gogotsi, and H. N. Alshareef, All pseudocapacitive MXene-RuO_2 asymmetric supercapacitors, Adv. Energy Mater. **8**, 1703043 (2018).

[140] Y. Wu, H. Hu, C. Yuan, J. Song, and M. Wu, Electrons/ions dual transport channels design: Concurrently tuning interlayer conductivity and space within re-stacked few-layered MXenes film electrodes for high-areal-capacitance stretchable micro-supercapacitor-arrays, Nano Energy **74**, 104812 (2020).

[141] X. He, T. Bi, X. Zheng, W. Zhu, and J. Jiang, Nickel cobalt sulfide nanoparticles grown on titanium carbide MXenes for high-performance supercapacitor, Electrochim. Acta **332**, 135514 (2020).

[142] W. Guo, C. Yu, S. Li, and J. Qiu, Toward commercial-level mass-loading electrodes for supercapacitors: Opportunities, challenges and perspectives, Energy Environ. Sci. **14**, 576 (2021).

[143] S. W. Bokhari, A. H. Siddique, P. C. Sherrell, X. Yue, K. M. Karumbaiah, S. Wei, A. V. Ellis, and W. Gao, Advances in graphene-based supercapacitor electrodes, Energy Rep. **6**, 2768 (2020).

[144] Y. Tian, G. Zeng, A. Rutt, T. Shi, H. Kim, J. Wang, J. Koettgen, Y. Sun, B. Ouyang, T. Chen, Z. Lun, Z. Rong, K. Persson, and G. Ceder, Promises and challenges of next-generation "beyond Li-ion" batteries for electric

vehicles and grid decarbonization, Chem. Rev. **121**, 1623 (2021).
[145] M. Walter, M. V. Kovalenko, and K. V. Kravchyk, Challenges and benefits of post-lithium-ion batteries, New J. Chem. **44**, 1677 (2020).
[146] C.-X. Zu and H. Li, Thermodynamic analysis on energy densities of batteries, Energy Environ. Sci. **4**, 2614 (2011).
[147] E. D. Alves, D. X. de Andrade, A. R. de Almeida, and G. Colherinhas, Atomistic molecular dynamics study on the influence of high temperatures on the structure of peptide nanomembranes candidates for organic supercapacitor electrode, J. Mol. Liq. **334**, 116126 (2021).
[148] Z. Bo, C. Li, H. Yang, K. Ostrikov, J. Yan, and K. Cen, Design of supercapacitor electrodes using molecular dynamics simulations, Nano-Micro Lett. **10**, 1 (2018).
[149] S. Datta, *Quantum Transport: Atom to Transistor* (Cambridge University Press, Cambridge, UK, 2005).
[150] K. H. Bevan, A. Roy-Gobeil, Y. Miyahara, and P. Grutter, Relating Franck-Condon blockade to redox chemistry in the single-particle picture, J. Chem. Phys. **149**, 104109 (2018).
[151] T. D. Kühne, M. Iannuzzi, M. Del Ben, V. V. Rybkin, P. Seewald, F. Stein, T. Laino, R. Z. Khaliullin, O. Schütt, and F. Schiffmann *et al.*, CP2K: An electronic structure and molecular dynamics software package-Quickstep: Efficient and accurate electronic structure calculations, J. Chem. Phys. **152**, 194103 (2020).
[152] M. Krack, Pseudopotentials for H to Kr optimized for gradient-corrected exchange-correlation functionals, Theor. Chem. Acc. **114**, 145 (2005).
[153] J. Spencer and A. Alavi, Efficient calculation of the exact exchange energy in periodic systems using a truncated coulomb potential, Phys. Rev. B **77**, 193110 (2008).
[154] G. Kresse and J. Hafner, Ab initio molecular dynamics for liquid metals, Phys. Rev. B **47**, 558 (1993).
[155] G. Kresse and J. Furthmüller, Efficiency of ab-initio total energy calculations for metals and semiconductors using a plane-wave basis set, Comput. Mater. Sci. **6**, 15 (1996).
[156] G. Kresse and J. Hafner, *Ab initio* molecular-dynamics simulation of the liquid-metal–amorphous-semiconductor transition in germanium, Phys. Rev. B **49**, 14251 (1994).
[157] J. Paier, M. Marsman, K. Hummer, G. Kresse, I. C. Gerber, and J. G. Ángyán, Screened hybrid density functionals applied to solids, J. Chem. Phys. **124**, 154709 (2006).
[158] J. P. Perdew, K. Burke, and M. Ernzerhof, Generalized Gradient Approximation Made Simple, Phys. Rev. Lett. **77**, 3865 (1996).
[159] G. Kresse and D. Joubert, From ultrasoft pseudopotentials to the projector augmented-wave method, Phys. Rev. B **59**, 1758 (1999).
[160] P. E. Blöchl, Projector augmented-wave method, Phys. Rev. B **50**, 17953 (1994).
[161] K. Momma and F. Izumi, VESTA 3 for three-dimensional visualization of crystal, volumetric and morphology data, J. Appl. Crystallogr. **44**, 1272 (2011).
[162] S. P. Ong, W. D. Richards, A. Jain, G. Hautier, M. Kocher, S. Cholia, D. Gunter, V. L. Chevrier, K. A. Persson, and G. Ceder, Python materials genomics (pymatgen): A robust, open-source Python library for materials analysis, Comput. Mater. Sci. **68**, 314 (2013).
[163] H. Widjaja, M. Altarawneh, and Z.-T. Jiang, Trends of elemental adsorption on graphene, Can. J. Phys. **94**, 437 (2016).
[164] K. Nakada and A. Ishii, Migration of adatom adsorption on graphene using DFT calculation, Solid State Commun. **151**, 13 (2011).
[165] C. Arbizzani, M. Biso, D. Cericola, M. Lazzari, F. Soavi, and M. Mastragostino, Safe, high-energy supercapacitors based on solvent-free ionic liquid electrolytes, J. Power Sources **185**, 1575 (2008).
[166] T. Binninger, A. Marcolongo, M. Mottet, V. Weber, and T. Laino, Comparison of computational methods for the electrochemical stability window of solid-state electrolyte materials, J. Mater. Chem. A **8**, 1347 (2020).
[167] L. Yu and G. Z. Chen, Ionic liquid-based electrolytes for supercapacitor and supercapattery, Front. Chem. **7**, 272 (2019).
[168] A. F. Molina-Osorio, A. Gamero-Quijano, P. Peljo, and M. D. Scanlon, Membraneless energy conversion and storage using immiscible electrolyte solutions, Energy Stor. Energy Transform. **21**, 100 (2020).
[169] P. Navalpotro, C. Trujillo, I. Montes, C. M. S. S. Neves, J. Palma, M. G. Freire, J. A. P. Coutinho, and R. Marcilla, Critical aspects of membrane-free aqueous battery based on two immiscible neutral electrolytes, Energy Storage Mater. **26**, 400 (2020).
[170] M. O. Bamgbopa, Y. Shao-Horn, R. Hashaikeh, and S. Almheiri, Cyclable membraneless redox flow batteries based on immiscible liquid electrolytes: Demonstration with all-iron redox chemistry, Electrochim. Acta **267**, 41 (2018).
[171] M. O. Bamgbopa, S. Almheiri, and H. Sun, Prospects of recently developed membraneless cell designs for redox flow batteries, Renew. Sust. Energ. Rev. **70**, 506 (2017).
[172] K. K. Kar, *Handbook of Nanocomposite Supercapacitor Materials. I, Characteristics Characteristics*, Springer Series in Materials Science Vol. 300 (Springer International Publishing AG, Cham, 2020).
[173] K. K. Kar, *Handbook of Nanocomposite Supercapacitor Materials. III, Selection*, Springer Series in Materials Science, 0933-033X Vol. 313 (Springer, Cham, Switzerland, 2021).
[174] B. K. Deka, A. Hazarika, J. Kim, Y.-B. Park, and H. W. Park, Recent development and challenges of multifunctional structural supercapacitors for automotive industries, Int. J. Energy Res. **41**, 1397 (2017).
[175] A. Arya and A. L. Sharma, Electrolyte for energy storage/conversion (Li^+, Na^+, Mg^{2+}) devices based on PVC and their associated polymer: A comprehensive review, J. Solid State Electrochem. **23**, 997 (2019).